nature nanotechnology

SUPPLEMENTARY INFORMATION

DOI: 10.1038/NNANO.2014.112

Measurement of collective dynamical mass of Dirac fermions in graphene

Hosang Yoon, Carlos Forsythe, Lei Wang, Nikolaos Tombros, Kenji Watanabe, Takashi Taniguchi, James Hone, Philip Kim* and Donhee Ham*

* Corresponding authors. E-mails: donhee@seas.harvard.edu, pk2015@columbia.edu

Contents

1 Collective electrodynamics of graphene electrons

1.1 Collective dynamical mass of graphene electrons

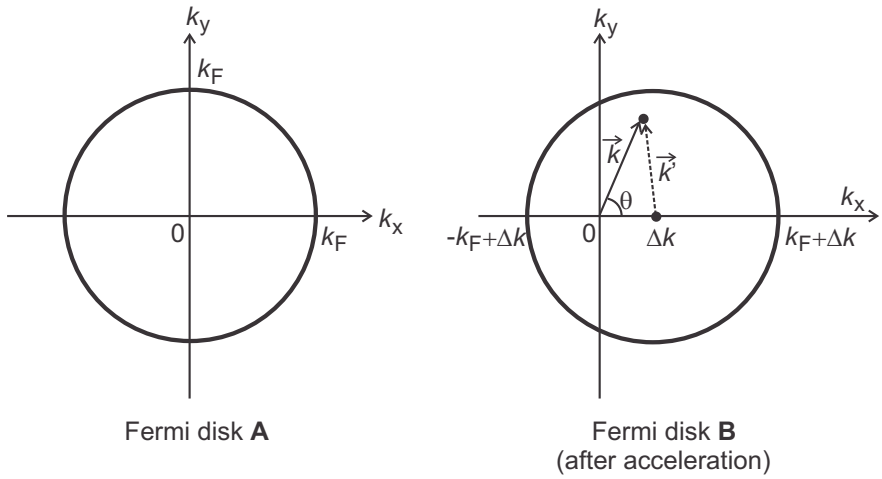

Supplementary Fig. 1: Fermi disks in the k-space.

Imagine a graphene strip of width W and a unit length, where electrons collectively move along the length towards the positive x-axis in response to an electric field. In the two-dimensional (2D) k-space (k: electron wavenumber), after a time duration Δt, the Fermi disk with a radius of Fermi wavenumber $k_{\rm F}$ and with its centre initially located at the origin [Supplementary Fig. 1; disk **A**] will have shifted toward the positive k_x-axis by Δk [Supplementary Fig. 1; disk **B**], producing a collective translational wavenumber per unit length, K, and a collective momentum per unit length, $P = \hbar K$:

$$K = n_0 W \Delta k; \tag{1}$$

$$P = n_0 W \hbar \Delta k, \tag{2}$$

where n_0 is the electron density per unit area. While $\Delta k \ll k_{\rm F}$, the shift is exaggerated in Supplementary Fig. 1.

The per-unit-length collective kinetic energy E corresponding to P is given by $E = E_{\mathbf{B}} - E_{\mathbf{A}}$, where $E_{\mathbf{A}}$ [$E_{\mathbf{B}}$] is the total kinetic energy of disk **A** [disk **B**] obtained by summing the single

electron energy $\epsilon(\vec{k}) = \hbar v_{\rm F} k$ ($v_{\rm F}$: Fermi velocity, $k = |\vec{k}|$) for all electrons in disk $\mathbf{A}$ [disk $\mathbf{B}$], *i.e.*:

$$\begin{aligned} E_{\mathbf{A}} &= W \iint\limits_{\mathbf{A}} g \frac{dk_x}{2\pi}\frac{dk_y}{2\pi}\epsilon(\vec{k}) = \frac{W\hbar v_{\rm F}}{\pi^2}\iint\limits_{\mathbf{A}} dk_x dk_y k; \\ E_{\mathbf{B}} &= W \iint\limits_{\mathbf{B}} g \frac{dk_x}{2\pi}\frac{dk_y}{2\pi}\epsilon(\vec{k}) = \frac{W\hbar v_{\rm F}}{\pi^2}\iint\limits_{\mathbf{B}} dk_x dk_y k. \end{aligned} \tag{3}$$

Here $g = 4$ accounts for spin and valley degeneracy and $\vec{k} = (k_x, k_y)$. As $\vec{k}' = (k'_x, k'_y)$ in Supplementary Fig. 1 is equal to $\vec{k} - \Delta k \hat{u}_{k_x}$ ($\hat{u}_{k_x}$: unit vector along the k_x direction), we can write $E_{\mathbf{B}}$ above as

$$E_{\mathbf{B}} = \frac{W\hbar v_{\rm F}}{\pi^2}\iint\limits_{\mathbf{B}} dk'_x dk'_y |\vec{k}' + \Delta k \hat{u}_{k_x}| = \frac{W\hbar v_{\rm F}}{\pi^2}\iint\limits_{\mathbf{B}} dk'_x dk'_y \left[k'^2 + 2k'_x\Delta k + (\Delta k)^2\right]^{1/2}, \tag{4}$$

where $k' = |\vec{k}'|$. By expanding the integrand to the second order of Δk (which is the lowest surviving order, as seen shortly), we obtain

$$E_{\mathbf{B}} = \frac{W\hbar v_{\rm F}}{\pi^2}\iint\limits_{\mathbf{B}} dk'_x dk'_y \left[k' + \frac{k'_x}{k'}\Delta k + \frac{k'^2_y}{2k'^3}(\Delta k)^2\right]. \tag{5}$$

Since the first term on the right hand side is identical to $E_{\mathbf{A}}$ and the second term vanishes due to the odd symmetry of k'_x within disk $\mathbf{B}$, Eq. (5) is simplified to

$$E_{\mathbf{B}} = E_{\mathbf{A}} + \frac{W\hbar v_{\rm F}}{\pi^2}(\Delta k)^2 \iint\limits_{\mathbf{B}} dk'_x dk'_y \frac{k'^2_y}{2k'^3}. \tag{6}$$

Subsequently,

$$E = E_{\mathbf{B}} - E_{\mathbf{A}} = \frac{W\hbar v_{\rm F}}{\pi^2}(\Delta k)^2 \iint\limits_{\mathbf{B}} dk'_x dk'_y \frac{k'^2_y}{2k'^3}, \tag{7}$$

which can now be readily integrated:

$$E = \frac{W\epsilon_{\rm F}}{2\pi}(\Delta k)^2 = \frac{1}{2}\times\frac{\epsilon_{\rm F}}{\pi W n_0^2}\times K^2 = \frac{1}{2}\times\frac{\epsilon_{\rm F}}{\pi W n_0^2\hbar^2}\times P^2. \tag{8}$$

This quadratic dependency of E on the small enough Δk arises because E as a function of Δk assumes a smooth minimum when $\Delta k = 0$, *i.e.*, in the collective ground state.

So, while individual electrons with the linear ϵ-k dispersion ($\epsilon = \hbar v_{\mathrm{F}} k$) behave as massless particles, electrons in collective dynamics with the quadratic relation $E \propto (\Delta k)^2 \propto K^2 \propto P^2$ must exhibit a non-zero collective mass per unit length:

$$M = \frac{\pi W n_0^2 \hbar^2}{\epsilon_{\mathrm{F}}}, \tag{9}$$

with which Eq. (8) can be written as

$$E = \frac{\hbar^2 K^2}{2M} = \frac{P^2}{2M}. \tag{10}$$

The velocity v_{c} of the collection of electrons is then given by

$$v_{\mathrm{c}} = \frac{1}{\hbar}\frac{\partial E}{\partial K} = \frac{\hbar K}{M} = \frac{P}{M}. \tag{11}$$

As K increases with time, t, with force F (*e.g.*, due to the electric field considered here) applied to the collection of electrons in the graphene strip, v_{c} increases with t. Since $E = \int_0^t F v_{\mathrm{c}} dt = P^2/(2M)$, by differentiating this relation with respect to t, we obtain

$$\frac{d}{dt}(M v_{\mathrm{c}}) = F. \tag{12}$$

That is, the collective mass of electrons in graphene 'inertially' accelerates according to the Newton's 2nd law. Note the contrast between the collective velocity v_c and the individual electron velocity given by $1/\hbar \times \partial\epsilon/\partial k = v_{\mathrm{F}}$, which is constant even in the presence of the force F.

In sum, in graphene, while an individual electron behaves like a massless particle with a constant velocity v_{F}, electrons in collective excitation together exhibit a non-zero collective mass and a variable collective velocity v_{c} in keeping with the Newton's equation of motion. The emergence of the non-zero collective electron mass despite the zero individual electron mass in graphene sharply contrasts typical conductors where the non-zero individual electron effective mass m^* appearing

in the quadratic single electron energy dispersion $\epsilon = \hbar^2 k^2/(2m^*)$ is plainly multiplied by the total number of electrons to give collective mass. For instance, consider a unit-length strip (width W) of GaAs/AlGaAs 2D electron gas (2DEG). We can repeat the calculation above but with $\epsilon = \hbar^2 k^2/(2m^*)$ and with $g = 2$ (spin degeneracy) to obtain $E = W\hbar^2 k_{\rm F}^2/(4\pi m^*) \times (\Delta k)^2$. By using[1] $k_{\rm F}^2 = 2\pi n_0$ and P still given by Eq. (2), we can see $E = 1/2 \times 1/(W n_0 m^*) \times P^2$, *i.e.*, the collective mass per unit length is m^* multiplied by the total number of electrons contained in the unit-length GaAs/AlGaAs 2DEG.

To get a feel for how large the collective mass of electrons in graphene is, we can *operationally* calculate the collective mass *per electron*: $m_{\rm c}^* = M/(W n_0) = \epsilon_{\rm F}/v_{\rm F}^2$. For $\epsilon_{\rm F} = 0.1$ eV, $m_{\rm c}^* = 0.02 m_0$ ($m_0 = 9.1 \times 10^{-31}$ kg). For comparison, in GaAs/AlGaAs 2DEG, $m^* = 0.067 m_0$.

1.2 Relation of collective dynamical mass to kinetic inductance

Current I corresponding to E and $P = \hbar K$ is given by

$$I = W \iint_{\mathbf{B}} g \frac{dk_x}{2\pi} \frac{dk_y}{2\pi} e v_x(\vec{k}), \tag{13}$$

where $v_x(\vec{k})$ is the x-component of the velocity of an electron with wave vector $\vec{k}$. As any single electron velocity in graphene is $v_{\rm F}$, $v_x(\vec{k}) = v_{\rm F} \cos\theta$, with θ in reference to Supplementary Fig. 1. Thus,

$$I = \frac{W e v_{\rm F}}{\pi^2} \iint_{\mathbf{B}} dk_x dk_y \cos\theta = \frac{W e v_{\rm F}}{\pi^2} \int_0^{2\pi} d\theta \cos\theta \int_0^{k_{\rm F} + \Delta k \cos\theta} k dk, \tag{14}$$

where the distance between the origin and the edge of disk $\mathbf{B}$ at angle θ is approximated as $k_{\rm F} + \Delta k \cos\theta$, given $\Delta k \ll k_{\rm F}$. By performing the integration up to the first order of Δk (the lowest surviving order), we obtain

$$I = \frac{W e \epsilon_{\rm F}}{\pi \hbar} \Delta k. \tag{15}$$

[1] In GaAs/AlGaAs 2DEG where $g = 2$, $k_{\rm F}^2 = 2\pi n_0$; in graphene where $g = 4$, $k_{\rm F}^2 = \pi n_0$

Since $I \propto \Delta k$ and $E \propto (\Delta k)^2$, $E \propto I^2$. Specifically, from Eqs. (S15) and (S8), we can see that

$$E = \frac{1}{2} \times \frac{\pi\hbar^2}{We^2\epsilon_{\mathrm{F}}} \times I^2. \tag{16}$$

In analogy to the energy of a magnetic inductor with current I being $1/2 \times$ (magnetic inductance) $\times$ I^2, we identify the second factor of Eq. (16) as the per-unit-length kinetic inductance of graphene:

$$L_{\mathrm{k}} = \frac{\pi\hbar^2}{We^2\epsilon_{\mathrm{F}}} = \frac{\sqrt{\pi}\hbar}{We^2 v_{\mathrm{F}}} \times \frac{1}{\sqrt{n_0}}. \tag{17}$$

In fact, this kinetic inductance links the voltage V (that produces the electric field and moves the electrons) and the current I in exactly the same *mathematical* manner as magnetic inductance links voltage across it and current through it, *viz.*, $V = L_{\mathrm{k}}(dI/dt)$. To demonstrate, one can note that $E = \int_0^t VIdt = L_{\mathrm{k}}I^2/2$ and differentiate this equation with respect to time t. Since $E \propto (\Delta k)^2$ that was responsible for the emergence of M now gives rise to L_{k}, M and L_{k} are two different representations of the same physics, with their intimate relationship given by

$$L_{\mathrm{k}} = \frac{M}{e^2 n_0^2 W^2}. \tag{18}$$

In fact, just as magnetic inductance represents the reluctance of magnetic flux to change, the kinetic inductance represents the 'inertial' reluctance of the collective momentum to change.

Typical conductors with the quadratic single electron ϵ-k dispersion also exhibit kinetic inductance arising from their more obvious collective electron mass, and $L_{\mathrm{k}} \propto 1/n_0$. By contrast, in graphene, $L_{\mathrm{k}} \propto 1/\sqrt{n_0}$ [Eq. (17)]. This peculiarity of graphene results from the linear single electron ϵ-k dispersion; that is, while individual and collective behaviours of electrons in graphene exhibit vast difference with zero individual electron mass and non-zero collective electron mass, the values of the collective electron mass and kinetic inductance are directly affected by the single electron energy dispersion.

1.3 Link to graphene plasmonics - I

As described in the main text, the collective motion of electrons in graphene can be modelled using a transmission line of Supplementary Fig. 2 (this figure is the same as Fig. 1d of the main text, except that we here have removed R for simplicity); kinetic inductance L_k, geometric (or classical) capacitance C_c, quantum capacitance C_q, all per unit length, model the acceleration of the collective electron mass, Coulomb restoring force, and electron degeneracy restoring pressure, respectively. The overall per-unit-length capacitance C is then given by $C = C_\mathrm{c}C_\mathrm{q}/(C_\mathrm{c} + C_\mathrm{q})$ [Supplementary Fig. 2]. The graphene plasmonic velocity v_p (not to be confused with v_c) is then given by $v_\mathrm{p} = \omega/k_\mathrm{p} = 1/\sqrt{L_\mathrm{k}C}$ (k_p: plasmonic wavenumber). This directly leads to the same intraband graphene plasmonic dispersion relation as derived from the random phase approximation (RPA) [*Phys. Rev. B* **75**, 205418 (2007)], a more general framework for plasmonic dispersion relation calculation which subsumes, but does not explicitly involve, the collective mass or kinetic inductance. This consistency confirms the central role the kinetic inductance (thus the collective electron mass) plays in graphene plasmonic waves.

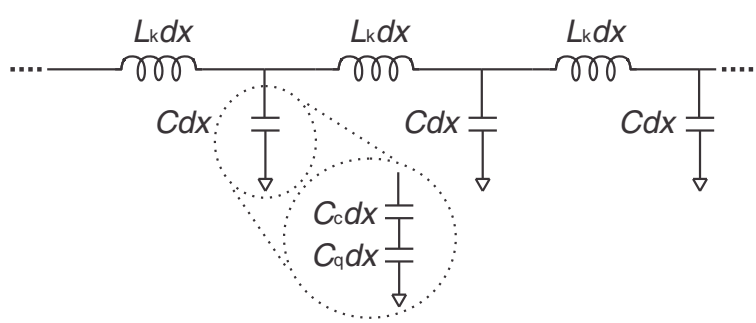

Supplementary Fig. 2: Lossless graphene transmission line.

Since C_c in Supplementary Fig. 2 varies with the electrostatic milieu, let us consider a specific example. In the case of ungated graphene, C_c for a given k_p may be expressed as $C_\mathrm{c} = 2\kappa\epsilon_0 k_\mathrm{p} W$ where κ is the effective dielectric constant of the surrounding medium [*Phot. Nano. Fund. Appl.* **10**, 166 (2012)]. The quantum capacitance C_q of graphene at low enough temperatures ($\epsilon_\mathrm{F} \gg k_\mathrm{B}T$) is $C_\mathrm{q} = 2We^2\epsilon_\mathrm{F}/(\pi\hbar^2 v_\mathrm{F}^2)$ [*Nat. Nanotechnol.* **4**, 505 (2009)]. Then the plasmonic dispersion relation for this ungated graphene is obtained from the transmission line model, *i.e.*, $v_\mathrm{p} = \omega/k_\mathrm{p} = 1/\sqrt{L_\mathrm{k}C}$

with $C = C_{\rm c}C_{\rm q}/(C_{\rm c}+C_{\rm q})$ and $L_{\rm k}$ of Eq. (17):

$$\omega = \frac{\epsilon_{\rm F}}{\hbar}\sqrt{2\alpha\left(\frac{k_{\rm p}}{k_{\rm F}}\right)+\frac{1}{2}\left(\frac{k_{\rm p}}{k_{\rm F}}\right)^2}, \tag{19}$$

where $\alpha \equiv e^2/4\pi\kappa\epsilon_0\hbar v_{\rm F}$. Importantly, this graphene plasmonic dispersion relation can be alternatively obtained with the RPA, using only the intraband propagator [*IEEE Trans. Nanotechnol.* **7**, 91 (2008)]. In Eq. (19), $C_{\rm c}$ affects only the first term inside the square root and $C_{\rm q}$ affects only the second term. Because $\alpha \sim 1$ in graphene on typical substrates, for small enough $k_{\rm p}$ (*i.e.*, $k_{\rm p} \ll k_{\rm F}$), the second term—the quantum capacitance effect—is negligibly small, and the dispersion relation of Eq. (19) reduces to [*Phys. Rev. B* **75**, 205418 (2007)]:

$$\omega = \frac{k_{\rm p}}{\sqrt{L_{\rm k}C}} = \frac{\epsilon_{\rm F}}{\hbar}\sqrt{2\alpha\left(\frac{k_{\rm p}}{k_{\rm F}}\right)}. \tag{20}$$

In this small $k_{\rm p}$-regime, $C_{\rm c} \ll C_{\rm q}$ and the restoring force is dominated by the Coulomb force while the electron degeneracy pressure is negligible. The dispersion relation of Eq. (20) in this regime has been experimentally demonstrated [*Nat. Nanotechnol.* **6**, 630 (2011)].

1.4 Link to graphene plasmonics - II

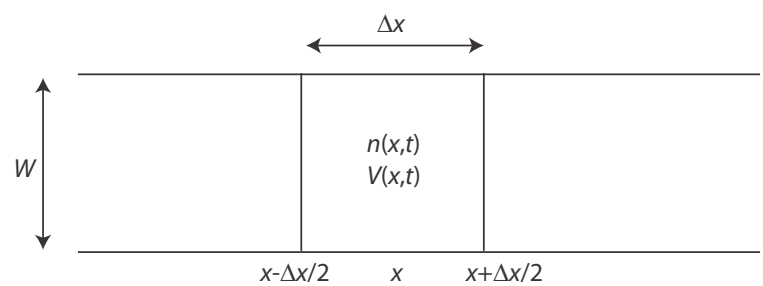

Supplementary Fig. 3: Electron density and potential distribution along a graphene strip where a plasmonic wave propagates along the length (x-axis). The infinitesimal length Δx is exaggerated.

We can visualize the link between the graphene plasmonic wave and the collective electron mass without using the circuit (transmission line) model, but by directly considering the dynamics of the collective electron mass in the presence of Coulomb restoring force and electron-degeneracy

restoring pressure. Imagine a plasmonic wave propagating along the length (x-axis) of the graphene strip. Let the potential and electron density of the infinitesimal segment of length Δx at position x be $V(x,t)$ and $n(x,t) = n_0 + \delta_n(x,t)$, respectively (Supplementary Fig. 3)[2], where $\delta_n(x,t)$ accounts for the extra (excess or deficit) electron density in this infinitesimal segment. The extra charge due to the extra electron density and potential $V(x)$ of the segment are related through its capacitance, $C\Delta x$, where $C = C_{\rm c}C_{\rm q}/(C_{\rm c} + C_{\rm q})$:

$$-eW\Delta x\delta_n(x,t) = C\Delta x V(x,t) \tag{21}$$

Since the restoring force (Coulomb force and the effect of electron degeneracy pressure) per unit positive charge is $-(\partial/\partial x)V(x,t)$, the restoring force that collectively drives the collection of electrons in the infinitesimal segment is given by:

$$F = -[-en(x,t)W\Delta x]\frac{\partial}{\partial x}V(x,t) = -\frac{e^2 n(x,t)W^2\Delta x}{C}\frac{\partial}{\partial x}\delta_n(x,t), \tag{22}$$

where we have used Eq. (21) in obtaining the last expression. With this force expression at hand, we now set up the equation of motion for the collection of electrons in the infinitesimal segment, according to Eq. (12):

$$\frac{\partial}{\partial t}[M(x,t)\Delta x v_{\rm c}(x,t)] = -\frac{e^2 n(x,t)W^2\Delta x}{C}\frac{\partial}{\partial x}\delta_n(x,t). \tag{23}$$

Here $v_{\rm c}(x,t)$ is the collective velocity of electrons in the infinitesimal segment and $M(x,t)$ is the per-unit-length collective electron mass at position x (thus $M(x,t)\Delta x$ is the collective electron mass of the infinitesimal segment). Given Eq. (9), $M(x,t)$ can be expressed as

$$M(x,t) = \frac{\pi W n^2(x,t)\hbar^2}{\epsilon_{\rm F}(x,t)}, \tag{24}$$

where $\epsilon_{\rm F}(x,t)$ is the Fermi energy corresponding to $n(x,t)$. Since $\delta_n(x,t) \ll n_0$ in any practical

[2]Here, the potential $V(x,t)$ is due not only to the Coulomb force, but also to the electron degeneracy pressure, that is, it combines the electric and quantum-mechanical potential.

situation, in the two equations above, we may use $n(x,t) \approx n_0$ and $\epsilon_{\rm F}(x,t) \approx \epsilon_{\rm F}$, where $\epsilon_{\rm F}$ is the previously defined equilibrium Fermi energy corresponding to n_0. Then Eq. (23) reduces to:

$$\frac{\partial}{\partial t} v_{\rm c}(x,t) = -\frac{1}{L_{\rm k} C n_0} \frac{\partial}{\partial x} \delta_n(x,t). \tag{25}$$

where we have used Eq. (17). On the other hand, as the total number of electrons is conserved, $v_{\rm c}(x,t)$ and $n(x,t)$ satisfy:

$$\frac{\partial}{\partial x}[n(x,t) v_{\rm c}(x,t)] = -\frac{\partial}{\partial t}[n(x,t)]. \tag{26}$$

By using $n(x,t) = n_0 + \delta_n(x,t)$ on both sides, but noting that $n(x,t)$ can be approximated as $n(x,t) \approx n_0$ on the left hand side, we obtain

$$n_0 \frac{\partial}{\partial x} v_{\rm c}(x,t) = -\frac{\partial}{\partial t} \delta_n(x,t). \tag{27}$$

By combining Eqs. (S25) and (S27), we obtain the following plasmonic wave equations:

$$\begin{aligned} \frac{\partial^2}{\partial x^2} \delta_n(x,t) &= L_{\rm k} C \frac{\partial^2}{\partial t^2} \delta_n(x,t); \\ \frac{\partial^2}{\partial x^2} v_{\rm c}(x,t) &= L_{\rm k} C \frac{\partial^2}{\partial t^2} v_{\rm c}(x,t). \end{aligned} \tag{28}$$

These plasmonic wave equations confirm $v_{\rm p} = \omega / k_{\rm p} = 1/\sqrt{L_{\rm k} C}$, which is the plasmonic dispersion relation previously obtained from the transmission line model and is consistent with the RPA approach in the intraband regime. This dynamic consideration once again attests to the physical reality of the collective electron mass, by directly delineating the machinery of the participation of the collective mass in the plasmonic wave propagation.

2 Comparison of kinetic and magnetic inductance in graphene devices

In the main text, we ignored the contribution of the magnetic inductance in setting up the high frequency model for the graphene channel because its magnitude is orders of magnitude smaller

than the kinetic inductance to be considered in the work. Also, we envisioned that the large kinetic inductance of graphene compared to its magnetic inductance may enable one to build inductors, ubiquitous in analogue integrated circuits but occupying large areas, in orders of magnitude smaller area. These can be more concretely seen in numbers in the following examples.

We first consider our own graphene device in Fig. 2 of the main text. In the graphene channel, the magnetic inductance would be formed in a parallel plate configuration (graphene and the top gate), whose value per unit length is given by $L_{\mathrm{m}} = \mu \frac{d}{W}$, where μ is the magnetic permeability, d is the distance between the plates, and W is the width of the plates. With $d \approx 200$ nm and $W = 7.5$ um in our device, this magnetic inductance per unit length evaluates to 3×10^{-3} pH/μm, while the kinetic inductance per unit length (kinetic inductance per square divided by the width, W) is measured to be at least around 10 pH/μm, 3 orders of magnitude larger than the magnetic inductance. Therefore, we can safely assume, in Fig. 1d of the main text or in Supplementary Fig. 2, that the inductance that we observe is dominantly caused by the kinetic inductance, with negligible contribution from the magnetic inductance.

As another example, we can consider the magnetic inductors prevalent in high frequency analogue integrated circuits that occupy very large chip area. For instance, in order to obtain 2.4 nH of inductance at GHz frequencies, ~ 4 mm^2 of chip area is needed [*IEEE J. Solid-State Circuits* **36**, 896 (2001)]. Taking the kinetic inductance per square of graphene as 100 pH/square (at ~ 5 V bias in Fig. 4a of the main text), with a graphene width of 10 μm, the same amount of inductance would be obtained in a 0.0024 mm^2 area, which is about 2600 times smaller than the magnetic inductor considered earlier. Such an application of using graphene as a kinetic inductor in analogue circuits may become a possibility as the mobility of CVD-grown graphene continues to improve.

3 Additional measurement results

3.1 s_{12} and s_{22} data in Fig. 3b,c

Fig. 3 of the main text displayed the s-parameters in terms of s_{21} and s_{11}, the transmission and reflection coefficients of electromagnetic waves incident from the left side of the device. In Supple-

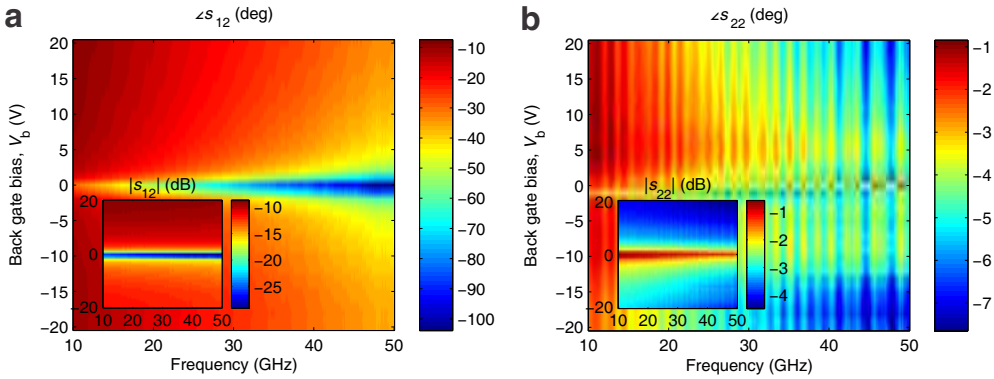

Supplementary Fig. 4: Phase (insets: amplitude) of the measured transmission (s_{12}; panel **a**) and reflection (s_{22}; panel **b**) parameters after the calibration and de-embedding at 30 K. These data are to be paired with Fig. 3b,c of the main text.

mentary Fig. 4, we present s_{12} and s_{22}, which correspond to the same transmission and reflection coefficients, but with the waves incident from the right side of the device. The results show that both the phases and amplitudes of s_{21} and s_{12}, and the amplitudes of s_{11} and s_{22} are almost identical. The phase of s_{22} shows slightly larger fluctuations with increasing frequency than that of s_{11}, but both are likely to be calibration/de-embedding artefacts (see Fig. 10 for the theoretically expected variation of s_{11} or s_{22} with frequency).

3.2 L_{k} measurements from an additional device

Here we present measurement results from another device in addition to the device appearing in the main text. The results confirm that the measurement and analysis presented in this work are clearly reproducible despite the difficult microwave measurement conditions detailed in the main text, owing to the h-BN encapsulation of graphene, one-dimensional edge contact, low temperature, and delicate microwave phase measurements.

Supplementary Fig. 5 shows the additional device's image and its DC 2-terminal resistance measurement result at 30 K. The device is relatively smaller ($W = 3.5$ μm, $l = 8.9$ μm) compared to the device in the main text, and shows a lower mobility of $\mu_{\mathrm{C}} = 85,000$ cm^2/Vs in the electron-doped region ($V_{\mathrm{b}} > V_{\mathrm{b,0}} = -2$ V). The hole-doped region ($V_{\mathrm{b}} < V_{\mathrm{b,0}}$) shows a much stronger asymmetric behaviour compared to the device in the main text, and therefore we focus our analysis on the electron-doped region where it functions as a clean graphene device.

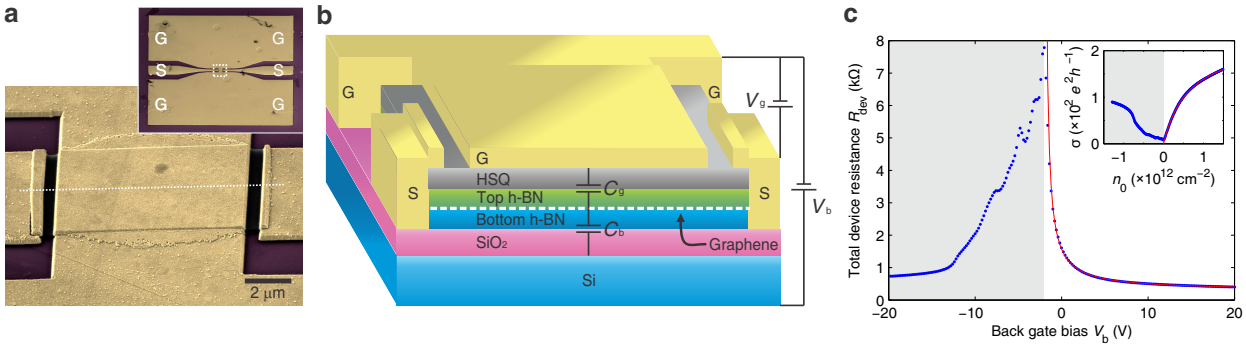

Supplementary Fig. 5: **a**, False coloured scanning electron micrograph of the additional device. The rough, rounded edges around the central rectangular region are artefacts from fabrication not important in the analysis. **b**, Schematic illustration of the device. Device dimensions are $W = 3.5$ μm, $l = 8.9$ μm, top h-BN thickness 43 nm, bottom h-BN thickness 13 nm, and HSQ thickness $\sim$ 100 nm. **c**, DC total device resistance R_{dev} measured at 30 K as a function of V_{b}, while graphene and the top gate are kept at the same DC potential, *i.e.*, $V_{\mathrm{g}} = 0$ (inset: corresponding conductivity plot; $n_0 = C_{\mathrm{b}}/W \times (V_{\mathrm{b}} - V_{\mathrm{b,0}})/e$ with $C_{\mathrm{b}}/W = 0.12$ fF/μm^2 and $V_{\mathrm{b,0}} = -2$ V). Red solid curves are fits to $\sigma^{-1} = (n_0 e \mu_{\mathrm{C}})^{-1} + \rho_{\mathrm{s}}$ with $\mu_{\mathrm{C}} = 85,000$ cm^2/Vs and $\rho_{\mathrm{s}} = 113$ Ω.

Supplementary Fig. 6 shows the results from microwave measurements performed with this device at 30 K. For this device, bias voltage is applied on the S-lines of the CPWs via bias tees (V_{g}), while the back gate was kept at the same DC potential as the top gate ($V_{\mathrm{b}} = 0$). This means the charge density induced on graphene is now expressed as $n_0 \approx (C_{\mathrm{b}} + C_{\mathrm{g}})/W \times (V_{\mathrm{g,0}} - V_{\mathrm{g}})/e$, as opposed to $n_0 \approx C_{\mathrm{b}}/W \times (V_{\mathrm{b}} - V_{\mathrm{b,0}})/e$ for the DC 2-terminal measurement. C_{g}/W is estimated to be roughly 0.22 fF/μm^2 from the thicknesses of the top h-BN and the HSQ layer. The microwave measurement results seen in Supplementary Fig. 6b,c are qualitatively similar to those obtained from the device in the main text (Fig. 3), amenable to L_{k} extraction.

Supplementary Fig. 7 shows the device model parameters (L_{k}, C_{g}, and R_{dev}) extracted from the microwave measurement data. The results are qualitatively and quantitatively very similar to the device in the main text. In the electron-doped region away from charge neutrality ($V_{\mathrm{g}} < V_{\mathrm{g,0}} = 1.2$ V; note the inverted direction due to the different biasing scheme in this measurement), extracted C_{g} stays nearly constant close to the expected value, extracted L_{k} closely follows the theoretically expected curve, and R_{dev} extracted from microwave measurements matches that measured at DC. The collective mass m_{c}^* obtained from L_{k} also closely follows the theoretically expected curve. We note that the standard errors in extracted L_{k} and C_{g} are relatively larger for

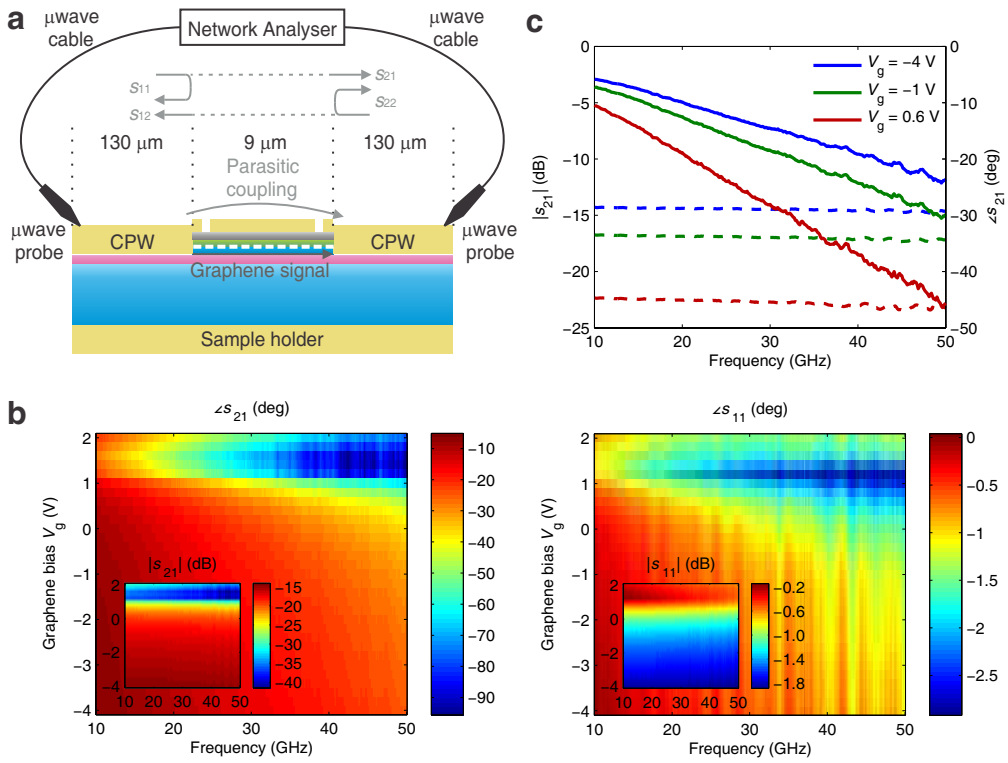

Supplementary Fig. 6: **a**, Schematic diagram of the measurement setup. The s-parameters shown are after calibrating out the delay and loss of the cables, probes, and on-chip CPWs, and also after de-embedding the parasitic coupling bypassing graphene. **b**, Phase (insets: amplitude) of the measured transmission (s_{21}; left) and reflection (s_{11}; right) parameters after the calibration and de-embedding at 30 K. For this device, bias voltage is applied on the S-lines of the CPWs via bias tees (V_{g}), while the back gate was kept at the same DC potential as the top gate ($V_{\mathrm{b}} = 0$). **c**, Select data from **b**, specifically, transmission phase ($\angle s_{21}$; solid curves) and amplitude ($|s_{21}|$; dashed curves) at three representative bias values V_{g} = -4, -1, and 0.6 V ($V_{\mathrm{b}} = 0$ V).

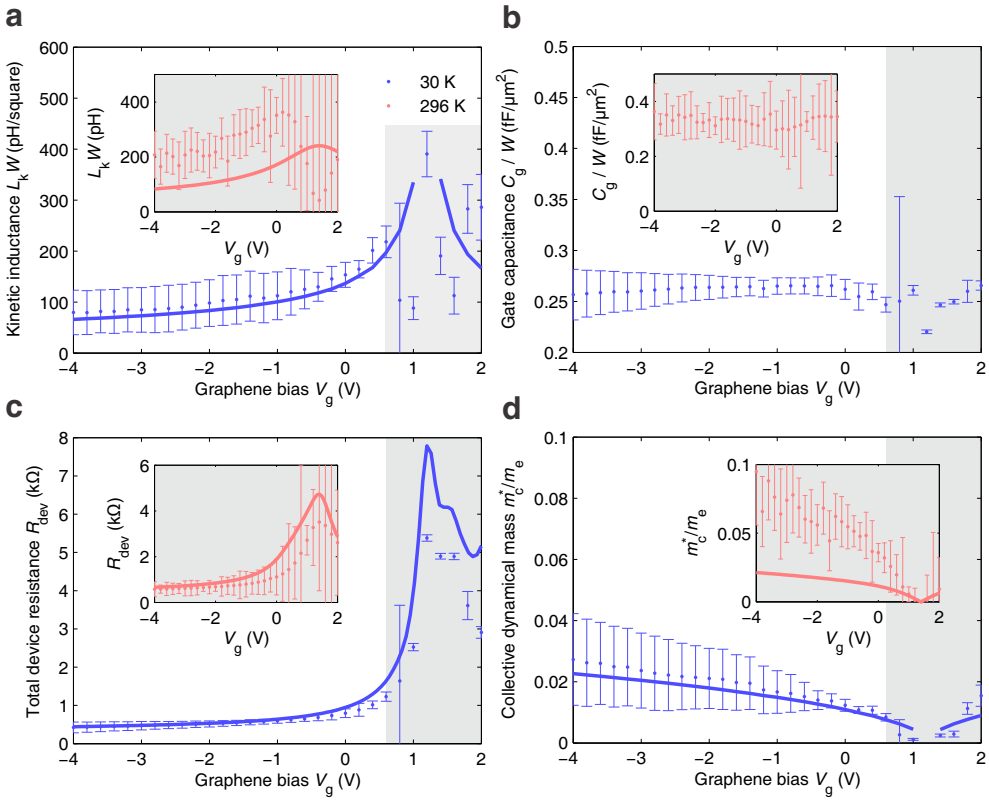

Supplementary Fig. 7: Kinetic inductance per square, $L_\mathrm{k}W$ (**a**), graphene to top-gate capacitance per area, C_g/W (**b**), total device resistance, R_dev (**c**), and collective dynamical mass per electron, m_c^* (**d**), extracted from the measured s-parameters for various V_g at 30 K and 296 K. The solid curves in **a** and **d** represent theoretical predictions. The solid curve in **c** is R_dev measured at DC (Supplementary Fig. 5c) but with the x-axis inverted and rescaled according to the ratio of the capacitance C_b relevant to the DC measurement of Supplementary Fig. 5c, to the capacitance $C_\mathrm{g} + C_\mathrm{b}$ relevant to the DC biasing in the microwave measurements. Error bars indicate standard errors of the extracted parameters (see Sec. 6.1).

the measurements of this device than those for the measurements of the device in the main text, which is to be expected as the mobility in this device is several times worse than the device of the main text. The qualitative and quantitative similarity of the measurement results of this device confirms that the measurement and analysis presented in this work are clearly reproducible despite the difficult microwave measurement conditions posed by in-graphene and contact resistances. The analysis in the following sections (Sec. 4, Sec. 5, Sec. 6) will be based on this device unless noted otherwise.

4 Phase delay $\phi(L_{\mathbf{k}}, C, R)$ and its device design implications

In the main text, the propagation phase delay ϕ expressed in terms of L_{k}, C, and R provided the key device design guideline (encapsulation of graphene with top and bottom h-BN layers, and proximate top gating) to enable the L_{k} measurement. Here we derive this ϕ expression, and elaborate more on the design guideline. As the electron scattering severely interferes with L_{k} measurement, we now consider the full graphene transmission line model of Fig. 1d of the main text, including per-unit-length resistance R modelling the electron scattering effect. For convenience, this lossy transmission line is re-produced in Supplementary Fig. 8.

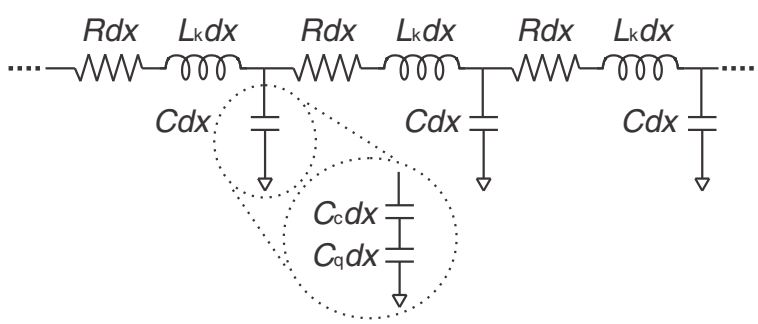

Supplementary Fig. 8: Lossy transmission line model for proximately gated graphene.

Let a wave of a microwave angular frequency ω propagating on the graphene transmission line be represented by the phasor $e^{-\gamma z}$ with the complex propagation factor $\gamma = \alpha + i\beta$ (α, β are real). γ's real part, α, captures the loss in the transmission line. Its imaginary part, β, is actually the plasmonic wavenumber k_p, as the wave in the graphene transmission line model considered here is

the graphene plasmonic wave. From the elementary theory of transmission line, γ is related to the transmission line's per-unit-length components, $L_{\rm k}$, C, and R, as follows:

$$\gamma = \alpha + i\beta = \sqrt{(R + i\omega L_{\rm k})(i\omega C)}. \tag{29}$$

The kinetic inductor's quality factor $Q = \omega L_{\rm k}/R$ is smaller than 1. Even after we substantially reduce R with the h-BN encapsulated structure and 30-K operation, Q ranges from 0.05 to 0.2 for the device of Supplementary Fig. 5 and from 0.2 to 0.8 for the device in the main text, as frequency is varied from 10 to 50 GHz; with graphene on a more standard substrate such as SiO_2, R is far larger and Q is even smaller. Therefore, we can approximate[3] the expression above to the first order of $Q = \omega L_{\rm k}/R$:

$$\alpha \approx \sqrt{\frac{\omega RC}{2}}\left(1 - \frac{1}{2}\frac{\omega L_{\rm k}}{R}\right); \tag{30}$$

$$\beta \approx \sqrt{\frac{\omega RC}{2}}\left(1 + \frac{1}{2}\frac{\omega L_{\rm k}}{R}\right). \tag{31}$$

The total propagation phase delay through the graphene transmission line of length l is βl, thus, the per-unit-length phase delay ϕ is no more than β, and we express it as in the main text:

$$\phi \approx \underbrace{\sqrt{\frac{\omega RC}{2}}}_{\phi_1} + \underbrace{\sqrt{\frac{\omega^3}{8}}\sqrt{\frac{C}{R}}L_{\rm k}}_{\phi_2}. \tag{32}$$

As seen, while the first term ϕ_1 is independent of $L_{\rm k}$, the second term ϕ_2 contains $L_{\rm k}$, thus, is of key interest; incidentally, their ratio is given by

$$\frac{\phi_2}{\phi_1} = \frac{1}{2}\frac{\omega L_{\rm k}}{R} = \frac{Q}{2}. \tag{33}$$

As described in the main text, decreasing R and increasing C are crucial for a given $L_{\rm k}$ to have a more 'measurable' impact on the phase delay ϕ (whose information is essentially included in

[3]The approximation, which may be inaccurate near 50 GHz for the device in the main text due to its large mobility, is used here to capture the most dominant effect affecting the measurements without complicating the algebra. However, no approximation is used in the extraction procedure (Sec. 6) to ensure accuracy.

the transmission coefficients s_{21} and s_{12}, which will be discussed in more detail in Sec. 5). The R-reduction proportionally improves $\phi_2/\phi_1 = Q/2$ and makes ϕ_2 a more appreciable fraction of ϕ_1, by reducing ϕ_1 and amplifying ϕ_2. The C-enhancement keeps ϕ_2/ϕ_1 constant, but still increases ϕ_2 itself. Taken together, the R-reduction and C-enhancement amplify ϕ_2 beyond the phase measurement error—which we call ϕ_e—caused by the imperfect calibration and non-ideal parasitic signal de-embedding[4]. Now, the criterion $\phi_2 > \phi_\mathrm{e}$ we have focused right above is necessary but not sufficient for L_k extraction. $\Delta\phi_2 > \phi_\mathrm{e}$ must be also satisfied, where $\Delta\phi_2$ is the variation of ϕ_2 corresponding to a target L_k extraction accuracy (resolution) ΔL_k, *i.e.*, $\Delta\phi_2 = \sqrt{\omega^3/8}\sqrt{C/R}\Delta L_\mathrm{k}$. To meet this additional criterion, we have to maximize $\Delta\phi_2/\Delta L_\mathrm{k} = \phi_2/L_\mathrm{k} \propto \sqrt{C/R}$, which is also achieved by the R-reduction and C-increase; in fact, the R-reduction and C-enhancement increased ϕ_2 above, by increasing the proportionality factor $\sqrt{C/R}$.

To substantially reduce R, we interface graphene with h-BN layers on both the top and bottom sides, and to obtain extra R-reduction, we also lower the operation temperature to 30 K in our main experiment. The C-enhancement is achieved by the proximate top gating. With the distance d between graphene and top gate being much smaller than graphene plasmonic wavelength $\lambda_\mathrm{p} = 2\pi/k_\mathrm{p}$ (*i.e.*, $k_\mathrm{p}d \ll 2\pi$, which is the case with our device), C_c of Supplementary Fig. 8 is just the parallel plate capacitance, $C_\mathrm{c} = \kappa\epsilon_0 W/d$, and with the effect of C_q negligible, $C = C_\mathrm{c} = \kappa\epsilon_0 W/d$. This is much larger than the capacitance of ungated graphene $2\kappa\epsilon_0 k_\mathrm{p} W$ (because $k_\mathrm{p}d \ll 2\pi$) mentioned in Sec. 1.3[5]. We can indefinitely increase C of our gated structure by keeping reducing d, but we stop at a certain point; in fact, we placed the extra layer of HSQ in addition to the top h-BN layer between graphene and top gate so that d is not too small. This is because with too large a C value, the attenuation constant $\alpha \propto \sqrt{C}$ of Eq. (30) would become too excessive, causing a significant attenuation. The C value chosen in our work is large enough to enable L_k extraction, but not so large so that we can maintain mild attenuation; $\alpha l \approx l\sqrt{\omega RC/2}$ ranges around $0.1 \sim 2$, depending on frequency ω and graphene bias V_g, as far as we keep away from the neutrality point,

[4]We also note that ϕ_e itself may decrease as C is increased as a result of better impedance matching of the graphene device to the measurement environment; see Eq. (35).

[5]In either our top gated case or the ungated case imagined here with our device, the back gate *un*connected to the G lines of the CPWs in our device is irrelevant as far as the microwave signalling is concerned, thus the capacitance C_b associated with the back gate does not come into our consideration here.

e.g., up to $V_{\mathrm{g}} \sim 0.6$ V.

5 Detailed analysis of s_{21}-parameters

To confirm that the C-enhancement and R-reduction indeed make the measured s-parameters amenable to L_{k} extraction, we analyse in details the measured transmission (s_{21}) parameters in Supplementary Fig. 6c in conjunction with simulations. In the foregoing section, we discussed the impact of the C-enhancement and R-reduction not on s_{21}'s phase ($\angle s_{21}$), but on the propagation phase delay ϕl. These two phase quantities are not exactly the same, because $\angle s_{21}$ takes into account not only ϕl, but also the phase change incurred by the reflection at the CPW-graphene interface[6]. Nonetheless, the behaviour of ϕl is strongly reflected in $\angle s_{21}$, and thus, the impact of C-enhancement and R-reduction on ϕl should be also distinctively observed from $\angle s_{21}$. With this understanding, in the analysis of the s_{21} parameters here, our language will not be too rigorous in distinguishing the two phase quantities; we seek to present the essence instead of the most rigorous analysis that complicates algebra.

To appreciate the impact of the C-increase and R-reduction on our ability to extract L_{k}, we compare the measured s_{21}-parameters to the s_{21}-parameters simulated under various scenarios. For the s-parameter simulation, we use Sonnet frequency-domain electromagnetic field solver, where the graphene is modelled as a two-dimensional conductor where its resistive and kinetic inductive impedances enter as simulation parameters. Its capacitance (and negligible magnetic inductance) is attained as part of the simulation outcome. Electromagnetic waves in the frequency range of 10-50 GHz are launched onto the CPWs in the simulator; the simulated response of the graphene

[6]More concretely, s_{21} can be approximated as the following, after ignoring multiple reflection effects and contact effects for simplicity [*Phys. Rev. E* **70**, 016608 (2004)]:

$$s_{21} \approx \frac{4R_0 Z_0}{(R_0+Z_0)^2} e^{-\alpha l} e^{-i\beta l}. \tag{34}$$

Here $R_0 = 50\ \Omega$ is the characteristic impedance of the measurement environment, and Z_0 is the characteristic impedance of the lossy graphene transmission line,

$$Z_0 = \sqrt{\frac{R+i\omega L_{\mathrm{k}}}{i\omega C}} \approx \sqrt{\frac{R}{2\omega C}} \left[\left(1+\frac{1}{2}\frac{\omega L_{\mathrm{k}}}{R}\right) - i\left(1-\frac{1}{2}\frac{\omega L_{\mathrm{k}}}{R}\right)\right]. \tag{35}$$

where the last expression is approximation to the first order of $Q = \omega L_{\mathrm{k}}/R$. As can be seen, $\angle s_{21}$ is not just $\phi l = \beta l$ but includes the phase change associated with the reflection, captured by the complex factor $4R_0 Z_0/(R_0+Z_0)^2$.

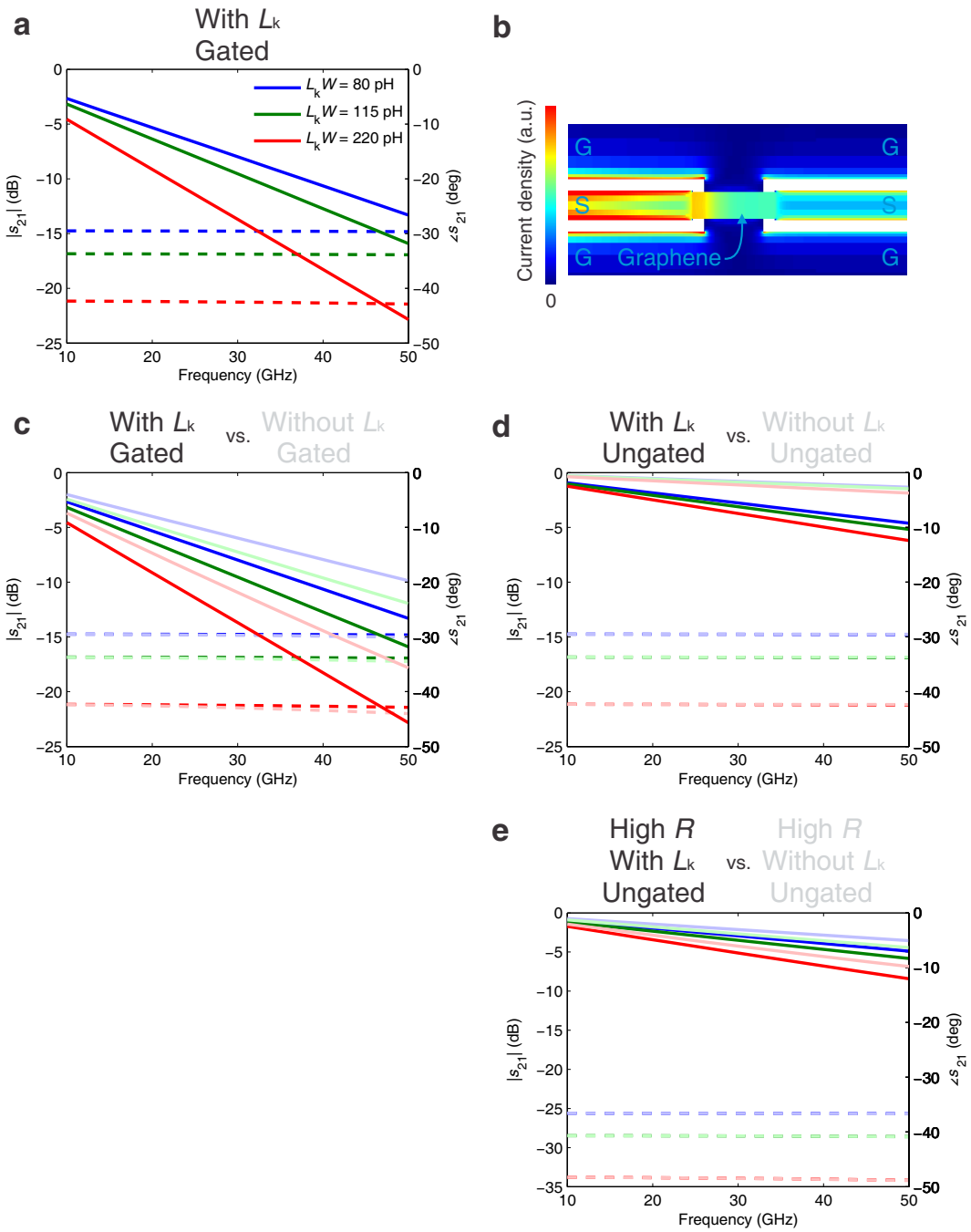

Supplementary Fig. 9: **a**, Simulated $\angle s_{21}$ (solid curves) and $|s_{21}|$ (dashed curves) for the gated h-BN interfaced graphene device in Supplementary Fig. 6 with $(L_kW,\ RW) = (80\text{ pH},\ 140\ \Omega)$ [blue], $(115\text{ pH},\ 200\ \Omega)$ [green], and $(220\text{ pH},\ 370\ \Omega)$ [red] per square, and contact resistances of 53 Ω on each side. **b**, Simulated current density distribution in the graphene layer at 50 GHz in the red-coloured case of **a**. **c**, Dark-coloured curves are identical to **a**; light-coloured curves are simulations without L_k in otherwise the same situation as **a**. **d**, Simulation results after removing the top gate from the case of **c**. **e**, Simulation results after increasing R by 5 times at each bias from the case of **d** (*i.e.* RW is 700 Ω [blue], 1,000 Ω [green], and 1,850 Ω [red] per square).

device is recorded in terms of s-parameters at each frequency.

1. **Reconstruction of the measured s_{21} of Supplementary Fig. 6c:** Supplementary Fig. 9a shows $\angle s_{21}$ (solid curves) and $|s_{21}|$ (dashed curves) simulated for our top-gated, h-BN encapsulated graphene device. This simulation is done with three sets of L_{k} and R values, extracted[7] from the measured s-parameters—whose s_{21} is in Supplementary Fig. 6c—at three different graphene bias (V_{g}) values. The simulated s_{21} of Supplementary Fig. 9a is almost identical to the measured s_{21} of Supplementary Fig. 6c. We can also examine the current distribution in the CPWs and graphene; a simulated graphene-layer current distribution example—corresponding to the red curves of Supplementary Fig. 9a at 50 GHz—is presented in Supplementary Fig. 9b, visualizing the signal propagation from the left CPW through graphene to the right CPW with attenuation.

2. **Impact of R-reduction in our device:** The dark-coloured simulated s_{21} curves of Supplementary Fig. 9c are the repetition of Supplementary Fig. 9a, but the light-coloured s_{21} curves of Supplementary Fig. 9c are simulated after removing L_{k} from the impedance parameter of graphene used in the simulation. The appreciable change in $\angle s_{21}$ curves after removing L_{k} at each bias reflects that the L_{k}-bearing ϕ_2 term is a measurable fraction of the L_{k}-independent ϕ_1 term. This is owing to the reduced R in our device.

3. **Impact of C-increase in our device:** The s_{21} curves in Supplementary Fig. 9d are simulated after removing the proximate top gate (thus with decreased C) in otherwise the identical simulation settings as Supplementary Fig. 9c. As seen in Supplementary Fig. 9d, even with the lower C, $\angle s_{21}$ curves before and after removing L_{k} at any given bias exhibit an appreciable difference, because C does not affect ϕ_2/ϕ_1 [Eq. (33)]. On the other hand, with C reduction, the progression of $\angle s_{21}$ with frequency (and thus $\angle s_{21}$ itself) substantially reduces—compare dark $\angle s_{21}$ curves between Supplementary Fig. 9c and Supplementary Fig. 9d. Consequently, without the top gate, the variation of $\angle s_{21}$ with varying values of L_{k} due to different graphene biases reduce to $\sim 1^\circ$ even at the highest frequency (dark $\angle s_{21}$ curves of Supplementary

[7] The extraction procedure will be fully detailed in Sec. 6.1.

Fig. 9d), while the phase measurement accuracy ϕ_e in our microwave measurement is typically limited to $\sim 1^\circ$ at best, due to the (inherently) imperfect calibration and non-ideal parasitic signal de-embedding[8]. This shows how the top gating and consequently larger C in our device enables L_k extraction.

4. **Impact of R-reduction in our device, once again:** The s_{21} curves of Supplementary Fig. 9e are simulated without top gating, just as in the case of Supplementary Fig. 9d, and now also with 5 times larger R value at each bias to emulate the situation of graphene interfaced with a more standard substrate (*e.g.* SiO_2/Si) and thus with reduced mobility. The already bad situation of Supplementary Fig. 9d is now even worsened in Supplementary Fig. 9e, where the dark-coloured $\angle s_{21}$ curves with L_k and light-coloured $\angle s_{21}$ curves without L_k at each bias become close with difference $\sim 1^\circ$ even at the highest frequency. This simulation once again demonstrates how the smaller R in our device helps L_k extraction.

5. **Behaviour of $|s_{21}|$:** So far we have focused on $\angle s_{21}$, but $|s_{21}|$ is also of importance. As can be seen in and across Supplementary Fig. 9c,d, $|s_{21}|$ is hardly affected by L_k or C but is almost solely determined by R. Specifically: when L_k is removed, $|s_{21}|$ at a given bias remains almost the same in either Supplementary Fig. 9c or Supplementary Fig. 9d; with differing C values between Supplementary Figs. 9c and 9d, $|s_{21}|$ at a given bias also remains practically the same; by contrast, both Supplementary Figs. 9c and 9d show that with increasing R with the varying graphene bias, $|s_{21}|$ conspicuously decreases. This R dependency of $|s_{21}|$ can be also seen by comparing Supplementary Fig. 9c,d with Supplementary Fig. 9e; with the 5 times larger R at any given bias, $|s_{21}|$ in Supplementary Fig. 9e is conspicuously smaller than $|s_{21}|$ in Supplementary Fig. 9c,d. Too small a value of $|s_{21}|$ as in Supplementary Fig. 9e (or near the charge neutrality point not discussed in this section) makes the de-embedding of graphene-bypassing parasitic signal highly error-prone, leading to spurious L_k, as will be discussed in Sec. 6. This is another reason why we should reduce R, hence the necessity of our h-BN graphene interface.

[8] Section 7 will present our experiment with an ungated graphene device, demonstrating the exceeding difficulty in L_k extraction from the s-parameters in the ungated case.

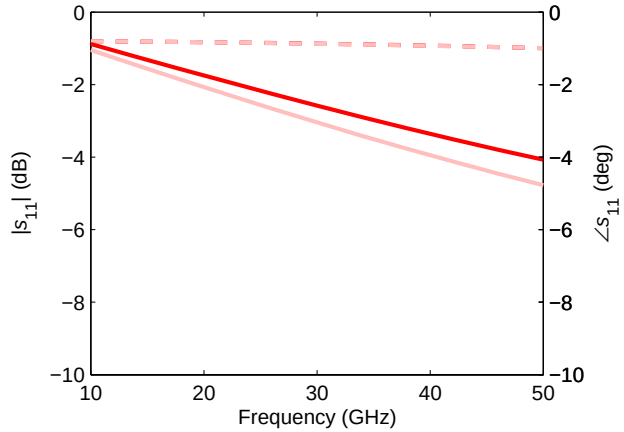

Supplementary Fig. 10: Simulated $\angle s_{11}$ (solid curves) and $|s_{11}|$ (dashed curves) with and without L_k (dark and light-coloured), which correspond to the dark and light red-coloured simulated s_{21} curves of Supplementary Fig. 9c.

In the above, we have shown how reduced R and increased C allow L_k to exert a more measurable impact on s_{21}. However, this does not mean that L_k can be extracted solely from s_{21} (and s_{12})[9]. While s_{21} certainly carries the information on L_k, L_k cannot be determined separately from C with s_{21} alone, because the effects of L_k and C are mixed in $\angle s_{21}$, and they have little impact on $|s_{21}|$. To determine L_k and C separately, we also need the reflection parameter s_{11} (and s_{22}).

We can see the effects of L_k and C on s_{11} from the Sonnet electromagnetic simulation of our top-gated, h-BN encapsulated graphene device; Supplementary Fig. 10 shows the simulated s_{11} with and without L_k (dark and light-coloured, respectively), which correspond to the dark and light red-coloured simulated s_{21} curves of Supplementary Fig. 9c. By comparison, we can see that while L_k and C had an additive effect on $\angle s_{21}$ (they both increased $\angle s_{21}$), they have a subtractive effect for $\angle s_{11}$ (C increases $\angle s_{11}$ but L_k decreases $\angle s_{11}$). Therefore, by combining $\angle s_{21}$ and $\angle s_{11}$ measurements, L_k and C can be separately determined.

[9] If our device is perfectly reciprocal, $s_{21} = s_{12}$; in reality, the perfect reciprocity is somewhat compromised, because the left and right contacts can behave differently.

6 L_{k} extraction from measured s-parameters

6.1 Procedure

Supplementary Fig. 11 shows the graphene transmission line model, plus the models for the left and right graphene contacts with the CPWs' S-lines. The left [right] contact model consists of $R_{\mathrm{con},1}$ [$R_{\mathrm{con},2}$] accounting for the contact resistance as well as the resistance of the small ungated graphene region near the left [right] contact seen in Fig. 2b,c of the main text or Supplementary Fig. 5a,b, $L_{\mathrm{ug},1}$ [$L_{\mathrm{ug},2}$] accounting for the kinetic inductance of the small ungated graphene region on the left [right], and capacitance $C_{\mathrm{con},1}$ [$C_{\mathrm{con},2}$] due to the small segment of the left [right] S-line edging over graphene. For a given set of model parameters (L_{k}, C, R and the contact model component parameters), we calculate the s-parameters using the transmission matrix method [Pozar, D. M. Microwave Engineering. (Wiley, 2004)]; this is a precise calculation, contrasting the approximate calculations that appeared in Secs. 4 and 5 to illustrate the physics of the measurement in a simple manner. The calculated model s-parameters consist of 8 sets of curves (real and imaginary parts of s_{11}, s_{21}, s_{12}, and s_{22}) that span the frequency range of 10-50 GHz. To determine L_{k} as well as other model parameters at a given bias, we repeat the calculation by altering the model component parameters until the calculated model s-parameters best fit—in the sense of least square curve fit, by using 'lsqcurvefit' function of MATLAB—the measured s-parameters at the bias all across the frequency range. Standard errors for the extracted parameters are obtained by supplying the final Jacobian of the fitting problem to the 'nlparci' function that can be configured to output the standard error of each parameter.

This optimization procedure requires a set of initial guesses for each model parameter. To ensure no arbitrariness, the same set of initial guesses were used across all the different sets of measurement data taken at varying bias voltages and temperatures for both the device in the main text and the device in Supplementary Fig. 5. These initial guesses are also very generic, taking values such as $L_{\mathrm{k}}W = 50$ pH, $Rl = 500\ \Omega$, and $Cl = 1$ fF. The fitting results are insensitive to the initial guesses; for instance, providing initial values 10$\sim$20 times away from the actual values does not alter the end result. The maximum and minimum bounds of the optimization range

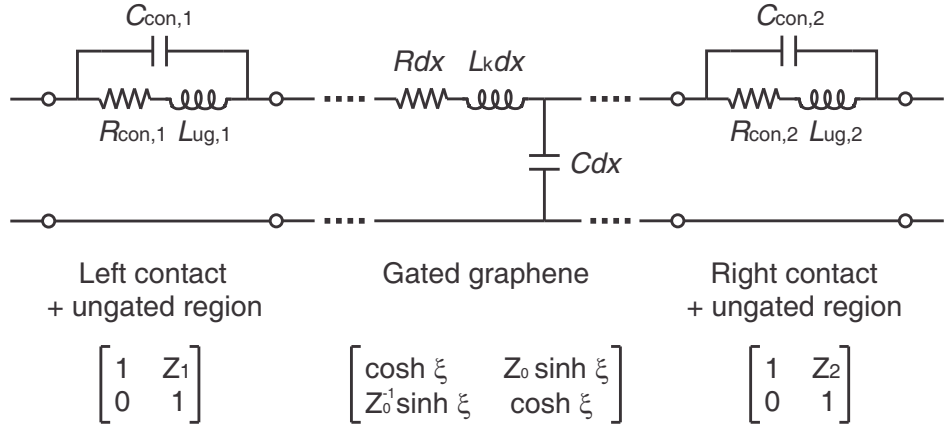

Supplementary Fig. 11: Model used to fit to the measured s-parameters. Corresponding transmission matrix representation is shown below. Here, $\xi = l\sqrt{(R+i\omega L_{\rm k})(i\omega C)}$ [dimensionless], $Z_0 = \sqrt{(R+i\omega L_{\rm k})/(i\omega C)}$ [Ω], and $Z_{1,2} = (R_{\rm con,1,2} + i\omega L_{\rm ug,1,2})||(1/i\omega C_{\rm con,1,2})$ [Ω]. R, $L_{\rm k}$, and C are per-unit-length variables whereas $R_{\rm con,1,2}$, $L_{\rm ug,1,2}$, and $C_{\rm con,1,2}$ are lumped variables.

for each model parameter, also needed by the 'lsqcurvefit' function, were set well away from the parameter's expected end value to ensure no interference with the arbitrarily set boundaries (*e.g.* $5\ \Omega \leq Rl \leq 50,000\ \Omega$, 0.5 pH $\leq L_{\rm k}W \leq 5000$ pH, 0.01 fF $\leq Cl \leq 100$ fF, etc.). These initial guesses and upper/lower bounds basically serve as a rough estimate of the order of magnitude that the parameters are expected to take for the 'lsqcurvefit' function to facilitate the curve fitting.

As an example, the final curve fits for the device data of Supplementary Fig. 7 at $V_{\rm g} = 0.6$ V (30 K) are shown in Supplementary Fig. 12. The final model s-parameters almost exactly match the measured s-parameters, attesting to the physical validity of the model of Supplementary Fig. 11. The fluctuations in the measured s-parameters in the higher frequency regions are due to residual parasitic signals and calibration errors; as these are not modeled by Supplementary Fig. 11, the model s-parameters do not generate such fluctuations. Device parameters so extracted are the $V_{\rm g} = 0.6$ V (30 K) data points in Supplementary Fig. 7. The rest data points of Supplementary Fig. 7 as well as Fig. 4 of the main text were obtained through exactly the same procedure.

6.2 Aberrant curve fit and extraction error

As seen in Fig. 4 of the main text or in Supplementary Fig. 7, the extracted $L_{\rm k}$ value deviates substantially from the theory near the charge neutrality point. In this regime, R is very large,

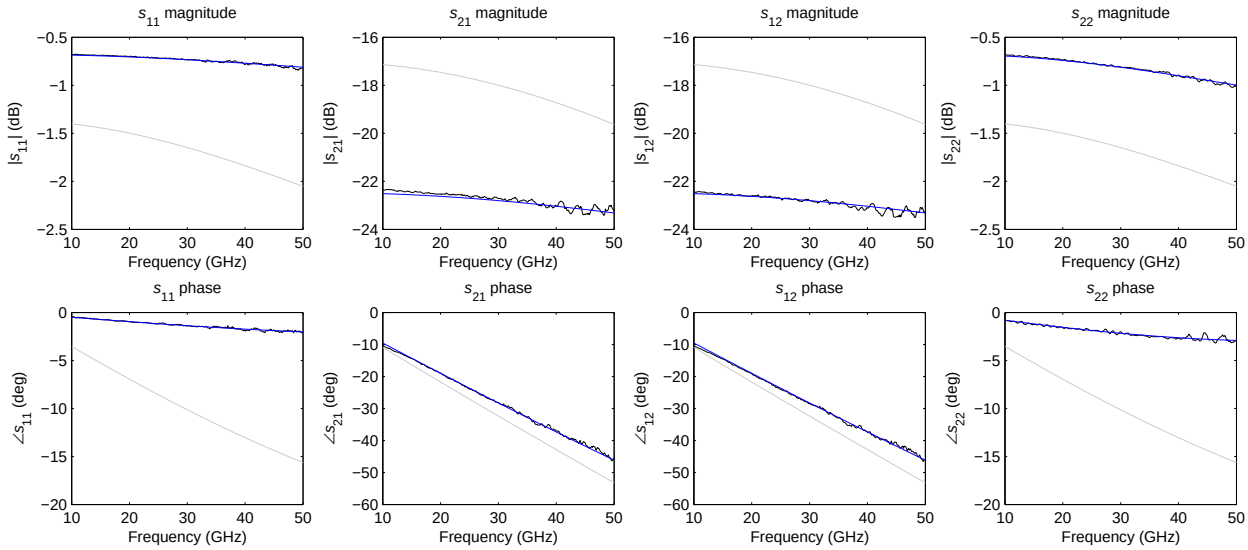

Supplementary Fig. 12: Measured (black) *vs.* fitted (blue) s-parameters for the device data of Supplementary Fig. 7 at $V_{\mathrm{g}} = 0.6$ V (30 K). Gray s-parameter curves obtained with the initially-guessed model parameters evolve to the blue curves as the optimization proceeds.

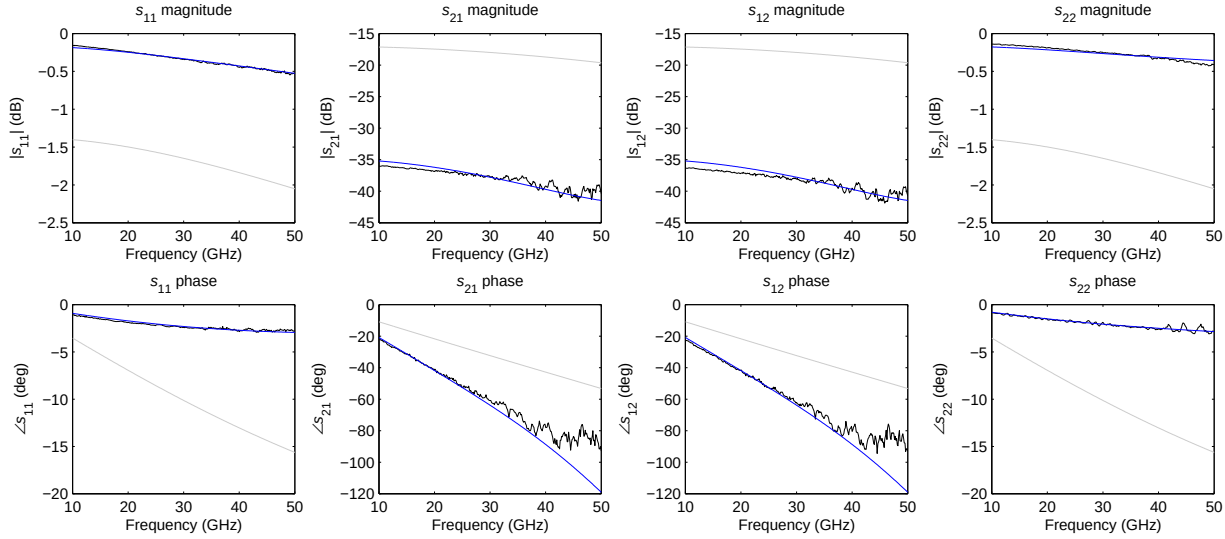

Supplementary Fig. 13: Measured (black) *vs.* fitted (blue) s-parameters for the device data of Supplementary Fig. 7 at $V_{\mathrm{g}} = 1.2$ V (30 K).

and the transmission through graphene is substantially lowered. Therefore, the *raw* s_{21} and s_{12} before removing the graphene-bypassing parasitic signal are dominated by the parasitic signal itself, rendering the parasitic-signal-de-embedded s_{21} and s_{12} highly distorted with residual parasitic signal. Since our model in Supplementary Fig. 11 does not take into account this residual parasitic signal, the final (best optimized with the least square curve fit) model s-parameters poorly fit the distorted s-parameters. For example, Supplementary Fig. 13 shows the finalized fitting for the s-parameters for the device data of Supplementary Fig. 7 at $V_{\mathrm{g}} = 1.2$ V (30 K); the finalized model s_{21} and s_{12} exhibit conspicuous deviation from the measured ones. This explains how the extracted L_{k} at $V_{\mathrm{g}} = 1.2$ V (30 K) in Supplementary Fig. 7 becomes spurious, causing its deviation from the prediction.

Even with the bias away from the charge neutrality point, at 296 K, the extracted L_{k} deviates from theory (Supplementary Fig. 7, insets or Fig. 4 of the main text). In this case, R is increased only by a few times compared to the 30-K case, thus, the detrimental residual parasitic signal effect is not as significant as near charge neutrality point, but the R-increase occurs for a fixed L_{k}, reducing both ϕ_2 and ϕ_2/ϕ_1. Consequently, measured s-parameters become once again more fraught with the measurement errors not modelled by Supplementary Fig. 11, rendering L_{k} extraction less accurate. The high sensitivity of our ability to reliably extract L_{k} on R stems from the fact that we are dealing with the sub-unit Q device.

We can quantify the fidelity of the curve fitting for a given type of s-parameter (*e.g.*, s_{21}) by summing the magnitude squared of the residual s-parameter fitting error normalized by the measured s-parameters' magnitude squared, over the measurement frequencies. This quantifies how well the model (Supplementary Fig. 11) is representing the measured data after the optimization. For s_{21}, this measure will be given by

$$e_{21}(V_{\mathrm{g}}) = \sum_i \frac{|s_{21,\mathrm{fitted}}(f_i, V_{\mathrm{g}}) - s_{21,\mathrm{measured}}(f_i, V_{\mathrm{g}})|^2}{|s_{21,\mathrm{measured}}(f_i, V_{\mathrm{g}})|^2}, \tag{36}$$

where the frequency f_i runs over the measurement frequencies. Supplementary Fig. 14 plots $e_{21}(V_{\mathrm{g}})$ and $e_{11}(V_{\mathrm{g}})$ for the data corresponding to Supplementary Fig. 7 at 30 K and 296 K. We first note that $e_{11}(V_{\mathrm{g}})$ is smaller than $e_{21}(V_{\mathrm{g}})$, as in our measurements, $|s_{21}|$ is much smaller than $|s_{11}|$,

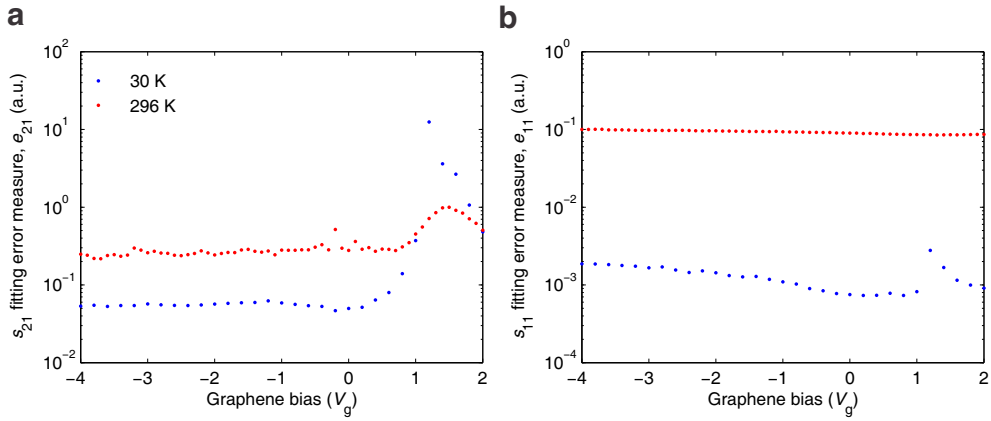

Supplementary Fig. 14: Plots of $e_{21}(V_\mathrm{g})$ and $e_{11}(V_\mathrm{g})$ for the data corresponding to Supplementary Fig. 7.

leaving s_{21} more prone to measurement errors. Next, we note that at 30 K, $e_{21}(V_\mathrm{g})$ is small away from the charge neutrality point, but becomes very large near the charge neutrality point (note the logarithmic scale); this is consistent with the degree of theory-measurement match of L_k shown in Supplementary Fig. 7. The worse theory-measurement match of L_k at 296 K as compared to 30 K (Supplementary Fig. 7) in the bias region away from the charge neutrality point is also consistently captured by the fact that $e_{21}(V_\mathrm{g})$ is larger for the 296 K data in this bias region. All in all, the fully consistent explanation of the sub-optimal-fitting in certain bias and temperature regimes furthers our confidence in the extracted L_k values in the regime where the fitting is optimal.

$e_{21}(V_\mathrm{b})$ and $e_{11}(V_\mathrm{b})$ calculated for the data corresponding to Fig. 4 in the main text show very similar behaviours. Specifically, 1) $e_{21}(V_\mathrm{b})$ is the smallest for the electron-doped region ($V_\mathrm{b} > V_{\mathrm{b},0}$) at 30 K where the extracted result was closest to the theory, 2) $e_{21}(V_\mathrm{b})$ shows a spike the near charge neutrality at both temperatures due to the distortion from parasitic signals, 3) $e_{21}(V_\mathrm{b})$ is larger overall for the 296 K data compared to the 30 K data due to the increase in R. Additionally, we can observe that $e_{21}(V_\mathrm{b})$ in the hole-doped region ($V_\mathrm{b} < V_{\mathrm{b},0}$) is conspicuously larger than that in the electron-doped region. This suggests that the microwave measurement data taken in the hole-doped region are distorted in a way that is inexplicable by the model of Supplementary Fig. 11, leading to a larger residual error after the optimization. Clean graphene device fabricated in an identical method[26] is expected to show a nearly symmetric in-graphene resistivity characteristic but the contacts show a highly asymmetric behaviour due to the work function mismatch between the metal

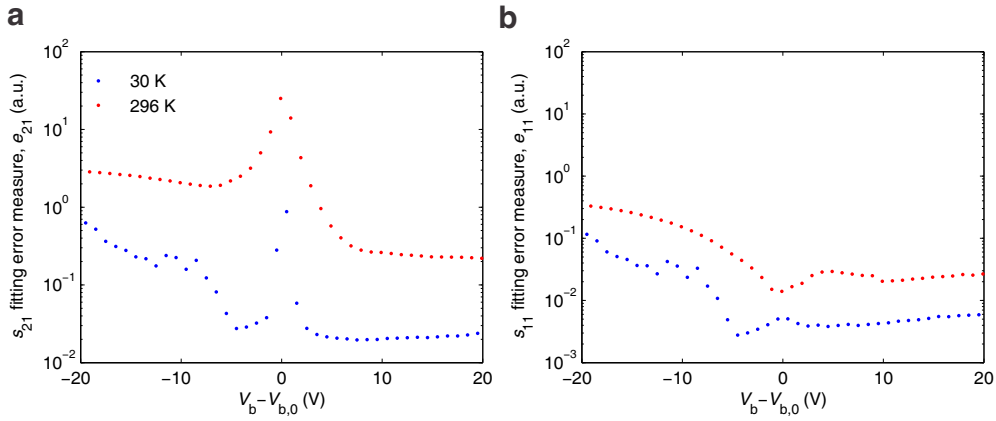

Supplementary Fig. 15: Plots of $e_{21}(V_\mathrm{b})$ and $e_{11}(V_\mathrm{b})$ for the data corresponding to Fig. 4 of the main text.

electrode and hole-doped graphene. Because hole-doped graphene is expected to exhibit exactly the same kinetic inductance and therefore exactly the same model for its microwave characteristics, we suspect that this distortion originates from the contact model of Supplementary Fig. 11 not being an accurate representation of the device with hole-doped graphene. More study will be needed to determine a high-frequency model for the one-dimensional edge contact of hole-doped graphene to metal electrodes that can more accurately describe the measured data.

7 Experiments with ungated, higher-resistance graphene

To further demonstrate how L_k measurement can fail without the strategies we employ (low graphene resistance + top gating), we here present experiments with an ungated graphene device with greater resistance. The optical image of this device is shown in Supplementary Fig. 16a, where the graphene strip ($W = 4.1$ μm, $l = 18.4$ μm) is visible. 2-terminal DC resistance measurement and analysis similar to those for Fig. 2 of the main text are performed at 296 K (Supplementary Fig. 16b). Charge neutrality occurs at $V_\mathrm{b} = V_{\mathrm{b},0} = -6.6$ V, with $\mu_\mathrm{C} = 8,000$ cm^2/Vs in the electron doped region ($V_\mathrm{b} > V_{\mathrm{b},0}$) and $\mu_\mathrm{C} = 26,000$ cm^2/Vs in the hole doped region ($V_\mathrm{b} < V_{\mathrm{b},0}$). This is considerably lower than the device of the main text, due both to the higher temperature and poorer innate sample quality. We also note that the contact resistance of ~ 2 kΩ in this device is several times worse than the device of the main text. The back gate capacitance is almost identical

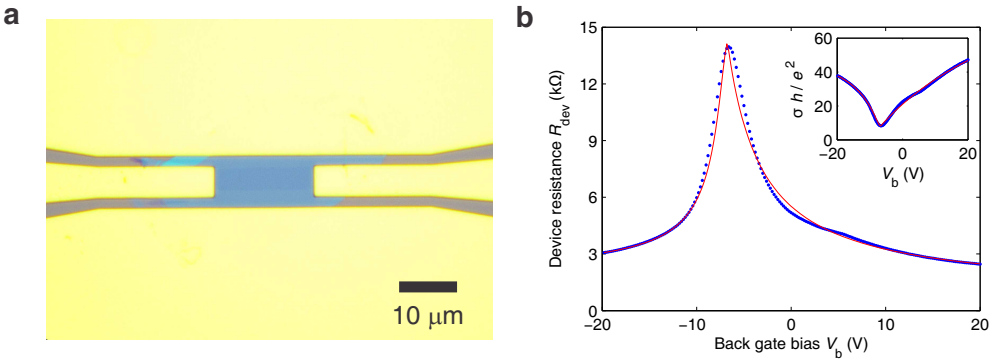

Supplementary Fig. 16: **a**, Optical image of an ungated graphene device. **b**, 2-terminal DC resistance measurement of the device at 296 K (inset: corresponding conductivity normalized to e^2/h).

to the device of the main text ($C_\mathrm{b} = 0.12$ fF/μm^2).

Microwave s-parameter measurements are performed in the same manner as the other devices. The DC biasing scheme for the microwave measurement is identical to the measurements in Supplementary Fig. 6, but only $C_\mathrm{b} = 0.12$ fF/μm^2 is relevant in determining n_0 in this case, as top gate is absent and the aforementioned ungated capacitance $2\kappa\epsilon_0 k_\mathrm{p} W$ is irrelevant to DC biasing. The results reveal that the device response suffers greatly from parasitic signals (Supplementary Fig. 17) due to the lower mobility and higher contact resistance in this device. Supplementary Fig. 17a,b show measured $|s_{21}|$ and $\angle s_{21}$ after calibration, but before removing the parasitic signals. We see that at certain biases ($V_\mathrm{g} = 0$ V), the device signal is almost completely buried in parasitic signals, while in other biases the signal is increasingly affected by parasitic signals at high frequencies where the parasitic signal magnitude is larger.

After de-embedding the parasitic signals (Supplementary Fig. 17c,d), a substantial deformation occurs to the measured $\angle s_{21}$ [compare to Fig. 3d of the main text], especially on the $V_\mathrm{g} = 0$ V data. Even the less distortion at $V_\mathrm{g} = 10$ V and 20 V is still quite detrimental. In addition, as graphene is not gated in this device, the substantial change in the graphene bias [red and green curves, Supplementary Fig. 9d] that must cause an appreciable change in L_k leads only to a small $\angle s_{21}$ difference of only a few degrees at best, further hampering L_k extraction. Device parameter extracted from these s-parameters are highly spurious (Supplementary Fig. 18), with the final curve fits for s-parameters plagued with large residual errors.

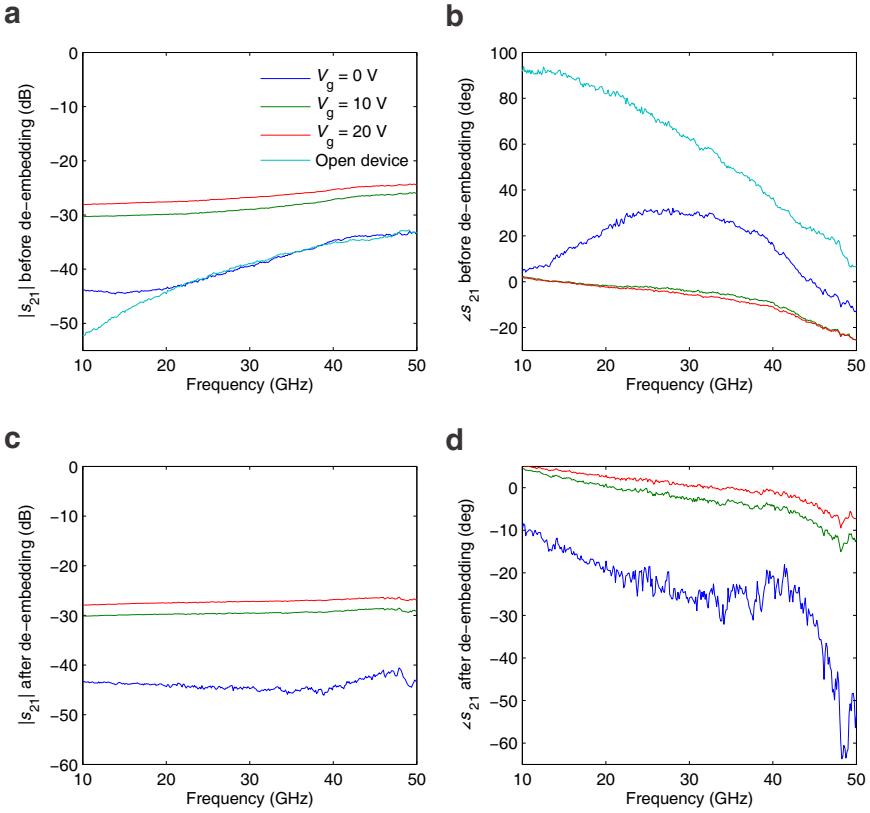

Supplementary Fig. 17: **a**, $|s_{21}|$ before parasitic signal de-embedding. **b**, $\angle s_{21}$ before de-embedding. **c**, $|s_{21}|$ after de-embedding. **d**, $\angle s_{21}$ after de-embedding.

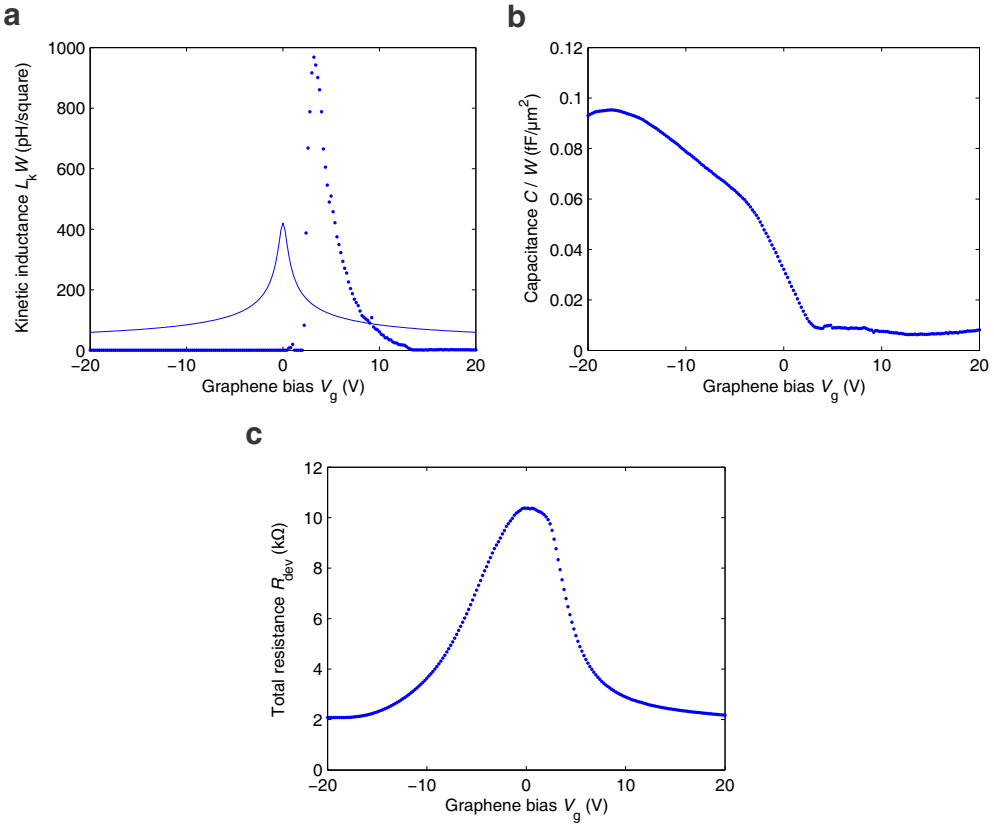

Supplementary Fig. 18: Kinetic inductance (**a**), capacitance (**b**), and total device resistance (**c**) extracted for the ungated graphene device. Solid curve in **a** is the theoretical prediction. This measurement was performed at a considerably later time compared to the DC measurement of Supplementary Fig. 16, and shows a conspicuous shift of the charge neutrality point.